Original Paper

Flow-visualization and numerical investigation on the optimum design of cavitating jet nozzle

Xiao-Ya Wu [a], Yi-Qun Zhang [a, *], Ya-Wen Tan [a], Gen-Sheng Li [a], Ke-Wen Peng [a, b], Bo Zhang [c]

[a] State Key Laboratory of Petroleum Resources and Prospecting, China University of Petroleum-Beijing, Beijing 102249, China
[b] Guangdong Provincial Key Laboratory of Distributed Energy Systems, Dongguan University of Technology, Dongguan 523808, Guangdong, China
[c] Department of Civil and Environmental Engineering, University of Alberta, Edmonton, Alberta T6G 2G7, Canada

ARTICLE INFO

ABSTRACT

Cavitating jet is widely used in drilling, rock cutting and ocean resource exploitation because of its strong erosion ability. The analysis of the relationship between the flow characteristics and the structure of cavitating jet nozzle is critical. Here, we utilized 3D printed technology and high-speed photography to design visualization experiments to analyse the impact of the variation of resonator and throat size of the organ-pipe self-resonating cavitating nozzles on the cavitation characteristics through image processing. The velocity field, pressure field and vapor volume fraction injected by the nozzle were taken as the objective functions to study the influence of different structural parameters on the cavitation effect based on FLUENT 19.0 software, and the results were compared with the experimental results. The results show that increasing the length and diameter of the resonator contributes to the occurrence of cavitation and the structure stability of the flow field. However, excessive size affects self-resonant of the nozzle and makes it difficult to form resonance effect. In this study, the optimal values of nozzle throat length and divergent angle are twice the throat diameter and 40°, respectively. This research provides an integrated research method to study the optimization of self-resonating nozzle and cavitating jet characteristics.
© 2022 The Authors. Publishing services by Elsevier B.V. on behalf of KeAi Communications Co. Ltd. This is an open access article under the CC BY license (http://creativecommons.org/licenses/by/4.0/).

1. Introduction

Cavitation, as a hydraulic phenomenon, was first found in the erosion damage of ship propeller with a history of more than 100 years (Chahine et al., 2014; Lindau et al., 2005). In essence, it belongs to phase transition, which refers to the phenomenon that when the liquid pressure is lower than the saturated vapor pressure, the liquid vaporizes and vapor bubbles are generated, then the vapor bubbles collapse due to instability (Liu et al., 2013). In the process of phase transformation, the bubble generally experiences initiation, development and collapse. The collapse process will be accompanied by high temperature, high pressure, micro-jet and sonoluminescence (Gaitan and Felipe, 1992) leading to severe erosion damage to the contact material surface, such as dykes, propellers and locks (Liao et al., 2020). Cavitation erosion can cause serious damage to these water conservancy facilities and instruments and generate huge economic losses (Peng C. et al., 2018).

Inversely, the failure characteristics of cavitation force can be used for rock breaking and borehole cleaning (Shen et al., 1996; Wu et al., 2003), which has a wide application in drilling and significantly improves penetration rate (Li and Shen, 1996; Wang et al., 2009).

Cavitating jet generated by self-resonating nozzle is an important way to utilize hydraulic cavitation energy (Li et al., 2016). The self-resonating cavitating nozzle triggers the inlet fluid oscillation by the feedback surface of the resonator. When the oscillation frequency is consistent with the natural frequency of the nozzle, resonance and standing wave are formed in the nozzle, and negative pressure is generated at the core zone of the nozzle. Compared with traditional contraction-expansion nozzles, self-resonating nozzles have stronger cavitation capacity and are more suitable for bottomhole confining pressure conditions (Li et al., 2003; Yi et al., 2005).

Ideally, when the hydraulic parameters of the jet are fixed, the natural frequency of the nozzle is corresponding to the jet excitation frequency. In field application, the nozzle structure is fixed but the hydraulic parameters shall be changed in a certain range. It is of great significance to study the influence of structure change in

---

* Corresponding author.
  E-mail address: zhangyq@cup.edu.cn (Y.-Q. Zhang).

nozzle size on cavitation performance. Cavitating jet has the characteristic of periodic fluctuation (Xiang et al., 2020; Peng K.W. et al., 2018). Cavitation bubbles can be observed to cluster into a cloud in the process of jet flow, and the cavitation cloud goes through four stages of initiation, development, shedding and collapse in a cycle (Peng et al., 2016). At the same position of flow field and different times, the corresponding cavitation cloud shape changes periodically, which makes the jet erosion ability fluctuate. The study of the periodic characteristics of cavitation jet is helpful to evaluate the capability of cavitating jet.

Cavitating jet experiments generally adopt the experimental scheme of high pump pressure and large displacement in the current studies. Based on hydrophone, the spectral characteristics of cavitation noise are studied following with the evaluation of cavitation effect (Cen et al., 2018). However, this experimental method produces severe cavitation phenomenon and obvious cavitation noise, which is easily affected by environmental noise and jet pump. In the jet images recorded by high-speed photography, problems of intense cavitation cloud, mixing disturbance of water bubbles can be observed. Cavitating jet simulation is usually carried out based on ANSYS FLUENT (Liu and Ma, 2021; Liu et al., 2020; Shi et al., 2019), while the development, migration, and collapse of cavitation bubbles are difficult to consider due to the difficulty of capturing the rule of changes for cavitation cloud morphology. Additionally, many studies of cavitating jet nozzle structure optimization are just from an experimental or simulation point of view, and the objective of optimization is not comprehensive. Therefore, in this paper, the combined method of visualization experiments and numerical simulation is employed to study the periodic distribution characteristics of cavitation clouds and the influence of nozzle structures on the cavitation clouds comprehensively.

In this study, the cavitating nozzle is processed by transparent resin 3D printing, and the cavitation initiation in the nozzle can be directly observed. In the experiment, the diameter of nozzle (1.5 mm), displacement rate (about 4 dm^3/min) and pump pressure (about 4 MPa) are minimized to clearly observe the change of cavitation cloud shape using high-speed photography. The power unit adopts magnetic gear pump, which has small pulsation, and the displacement can be stepless adjustable. It can be used to observe the minimum displacement of cavitation initiation and analyse the shape of initial cavitation cloud. The numerical simulation of cavitating jet is carried out by Fluent 19.0 software, and the flow field of cavitating jet under different structural parameters is analysed to obtain the performance variation rule of cavitating flow field in the nozzle. The influence of the change of nozzle structural parameters on the jet flow field is compared with cavitating jet experiments, and the rules of changes in the velocity, pressure and vapor volume fraction in the nozzle flow field are analysed. The optimal values of the nozzle structural parameters are selected based upon the visualization experiments and numerical simulation.

2. Experimental system and geometrical model

2.1. Experimental system

The schematic diagram of the cavitation jet experimental system is shown in Fig. 1 (Tan et al., 2022), mainly consisting of a magnetic gear pump, a throttle valve, a pressure and temperature sensor, a flow meter, a high-speed photography, a data acquisition system and a water tank. The water in the storage tank is filtered by the screen and flows to the self-resonating cavitating nozzle through the magnetic gear pump, throttle valve and pressure sensor to form the cavitating jet. The spotlight is on the same axis as the high-speed photography, and the data recorded by the flow

meter, pressure sensor and high-speed photography are transmitted to the data acquisition system for storage and correlation processing.

In order to photograph the specific details of the cavitating jet process, visualized cavitating jet experiments with low pump pressure and small displacement are designed. The experimental pump pressure is 4 MPa, and the displacement range is 4.7 L/min. The water jet medium is tap water at room temperature (300 K). The selection of high-speed photography parameters is important to the observation and feature acquisition of the flow field. When the exposure time is longer, the shot picture will be clearer and the number of frames recorded per second will be less. After sensitivity analysis of pre-shootings, the resolution is selected as 256 × 256 because it can clearly illustrate the cavitating flow field. The corresponding maximum frequency amplitude is 20000 FPS (20000 pictures/second), which can fully record the dynamic changes of cavitation cloud and distinguish different stages of cavitation jet process.

2.2. Geometrical model

The structure of the organ-pipe self-resonating nozzle is shown in Fig. 2, and the core design structure is the nozzle resonator and the nozzle throat. The nozzle structure design refers to the research results of scholars (Li and Shen, 1992), and the design of main parameters follows Eqs. (1)–(3).

$$L = \frac{K_N d}{MaSr},$$ (1)

$$K_N = \begin{cases} \frac{2N-1}{4}, & \left(\frac{D_s}{D}\right)^2 \gg 1, \left(\frac{D}{d}\right)^2 \gg 1 \\ \frac{N}{2}, & \left(\frac{D_s}{D}\right)^2 \gg 1, \left(\frac{D}{d}\right)^2 \gg 1 \end{cases},$$ (2)

$$Ma = \frac{v_j}{v_a},$$ (3)

where K_N is the modulus coefficient of vibration in the resonator; N is the oscillation modulus in the resonator; Ma is the Mach number of jet flow, dimensionless; v_j is the jet velocity; v_a is the propagation speed of sound waves in fluid medium; Sr is critical Strouhal number, dimensionless, with a value of 0.3 or 0.6.

The nozzle design results are as follows:

(1) The diameter of the nozzle throat is determined by the displacement range of the magnetic gear pump. In order to ensure the obvious occurrence of cavitation phenomenon, the diameter of the nozzle throat is designed to be 1.5 mm, and the jet velocity is greater than 60 m/s. Cavitation can occur under this condition of the pump output pressure.

(2) The length of the nozzle throat is designed to be 6 mm, following the settings of Peng et al. (2017).

(3) The diameter of the resonator is as follows: $\left(\frac{D}{d}\right)^2 \gg 1, D = 4$ mm.

(4) The diameter of the nozzle inlet is as follows: $\left(\frac{D_s}{D}\right)^2 \gg 1, D_s = 7.5$ mm.

(5) The length of the resonator is as follows: the nozzle structure shown in Fig. 2 indicates that the oscillation modulus of resonator $N = 1$; $K_N = 0.25$, which is derived from Eqs. (1)–(3). In order to ensure the smooth operation of the
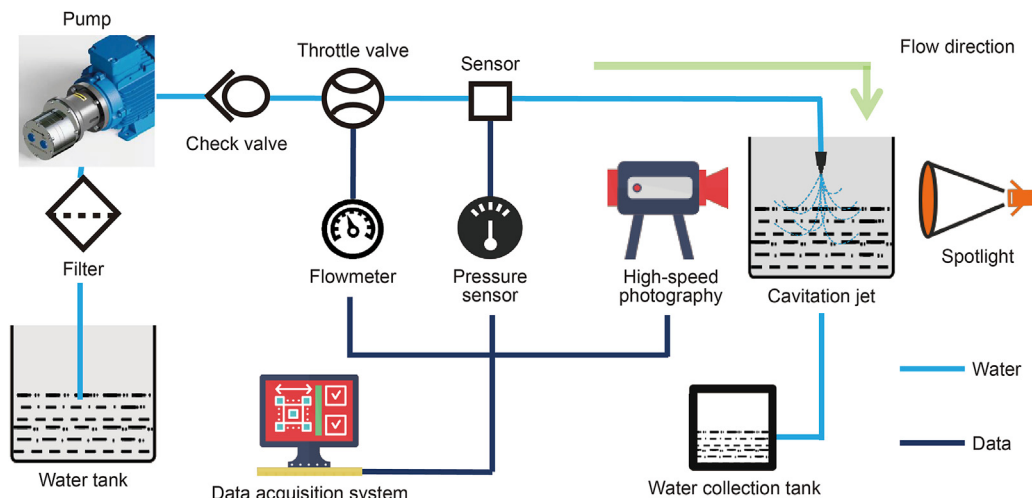
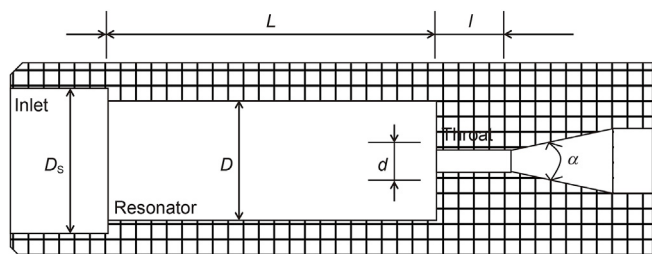**Fig. 1.** Cavitating jet experimental system.

Fig. 2. The self-resonating cavitating nozzle geometry (Li and Shen, 1992). D_s-Inlet diameter, D-Resonator diameter, d-Throat diameter, α-Divergent angle, L-Resonator length, l-Throat length.

experimental equipment, substitute v_j and Sr as 45 m/s and 0.3 into Eqs. (1) and (3) and derive that $L = 32$ mm.

The control group is designed based on the above designed nozzle. Four structure parameters, consisting of resonator diameter, divergent angle, resonator length, and throat length are selected as design variables. The design results are shown in Table 1.

2.3. Experimental data processing

The frame rate of 20000 FPS and frame width of 256×256 pixels are selected for high-speed photography. After the jet flow field is stabilized, 2000 images continuously recorded by high-speed photography are used as the experimental data at present displacement. Fig. 3 shows the main program of image differential processing in this study (Liu and Fang, 2004). Fig. 3(a) is the background of jet field, which mainly includes resonator, throat, extension section and the submerged environment outside the nozzle. Fig. 3(b) is the image at a certain moment recorded by high-speed photography in the process of jet flow. Fig. 3(c) illustrates the

difference between Fig. 3(a) and (b). For computer processing, the difference image (Fig. 3(c)) is converted into black and white binary image (the pixel value at black is 0, and the pixel value at white is 1). Fig. 3(d) is the difference image after binarization processing, which contains information including the change of jet field and some interference information. Fig. 3(e) is the difference image after removing the noise. Fig. 3(f) shows the binary difference after removing interference factors, and each frame corresponds to the experimental image.

Fig. 4 shows the processing principle of the dynamic change image of cavitation clouds. After background removal, binarization and noise reduction processing, the area where the cavitation clouds are located appears white on the image. The larger the average value of pixels per row, the closer the colour of the image is to white. Here, the range of the Y coordinate of the white pixel range in each image is defined as the dimensionless length of the cavitation cloud. Assuming that the cavitation cloud is spherical or cylindrical, the number of consecutive white pixels in each row of pixels represents the diameter of the corresponding cavitation bubble, and the sum of squares of each successive white pixel area in the whole image is defined as the dimensionless volume of the cavitation cloud.

3. Computational fluid dynamics (CFD) method and simulation

3.1. Governing equations

3.1.1. Multiphase model

Through the analysis of the flow characteristics of cavitation water jet under the condition of submerged environment, various vortex cavitation bubbles in the cavitation jet are observed. Therefore, the selection of an appropriate multiphase flow model is critical for the numerical calculation of cavitation jet.

Table 1
Structure design of organ-pipe cavitation nozzles.

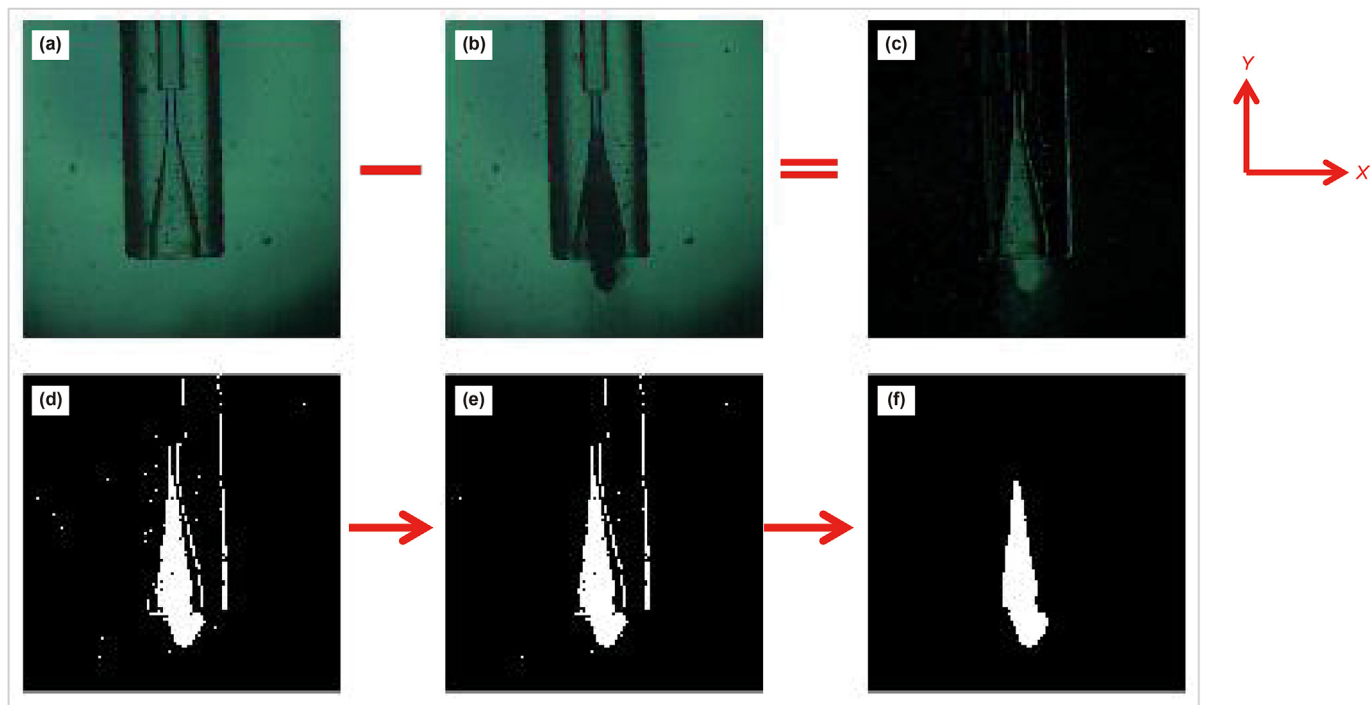| Throat diameter d, mm	Throat length l, mm	Resonator diameter D, mm	Resonator length L, mm	Divergent angle α, degree
1.5	1.5/3/6/9	4	32	25
1.5	6	2.5/4/5.5/7	32	25
1.5	6	4	16/24/32/40	25
1.5	6	4	32	10/25/40/55

Fig. 3. The program of image differential processing: (**a**) background image, (**b**) cavitating jet flow field, (**c**) background removed, (**d**) image binarization, (**e**) denoising, and (**f**) isolated line removed.
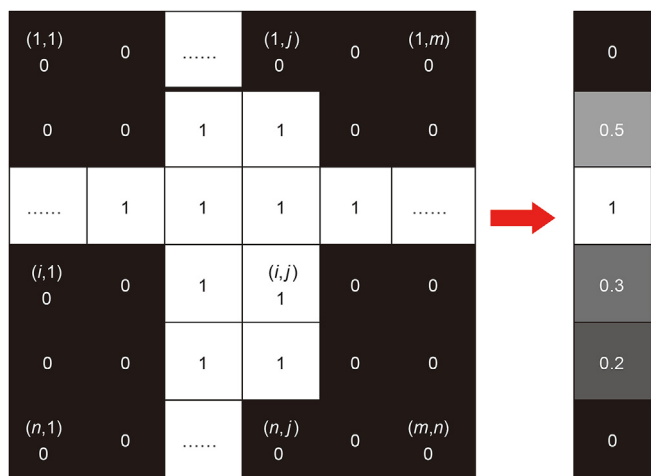

Fig. 4. Principle of image processing for the change of cavitation cloud.

VOF model is mainly applied to numerical calculation of gravity flow, free liquid surface flow, flow with large bubbles in the liquid and dam break, which can obtain the time-uniform distribution of the interface in the process of fluid flow (Peng and Shimizu, 2013). In this model, the volume average value is adopted for the viscosity and density of each phase, which requires the velocity of each phase in the system to meet the condition of equality. When the velocity difference is large, it will cause a large calculation error. However, the cavitation jet flow field studied in this paper is a complex system with mixed and doped phases, and there is a large velocity gradient at the jet boundary. Therefore, the VOF model, which tracks incompatible fluid interfaces, cannot meet the computational requirements.

Eulerian model needs to ensure the basic properties of each phase, so it requires to list the conservation equation of each phase instead of replacing it with the average value. This model has the highest computational accuracy among the three commonly used multiphase flow models (Chen et al., 2019). However, while improving the computational accuracy, it requires higher requirements on computer hardware, which leads to the limitation of the application of this model to a certain extent. Combined with the actual situation in the research process of this paper, it cannot meet the practical calculation needs.

Mixture model focuses on the whole mixed flow field system, which has the advantages of high accuracy, low resource occupancy and fast computational efficiency. This model is suitable for the calculation of cavitation characteristics in the cavitation jet flow field (Chen et al., 2018, 2019), so the mixture model is adopted as the multiphase model in this study.

The mixture continuity equation can be expressed as

$$\frac{\partial}{\partial t}(\rho_m) + \frac{\partial}{\partial x_j}(\rho_m u_j) = 0. \tag{4}$$

The momentum equation for the mixture model can be written as

$$\frac{\partial}{\partial t}(\rho_m u_i) + \frac{\partial}{\partial x_j}(\rho_m u_i u_j) = -\frac{\partial P}{\partial x_i} + \frac{\partial \tau_{ij}}{\partial x_j}, \tag{5}$$

where ρ_m is the mixture density; P is the mixture pressure; u_i and u_j are the velocity in the i and j directions, respectively; τ_{ij} denotes the viscous tensor, which can be expressed as

$$\tau_{ij} = (\mu_m + \mu_t)\left[\left(\frac{\partial u_i}{\partial x_j} + \frac{\partial u_j}{\partial x_i}\right) - \frac{2}{3}\delta_{ij}\frac{\partial u_k}{\partial x_k}\right], \tag{6}$$

where μ_m and μ_t are the molecular and turbulence viscosities obtained from the turbulence model, respectively.

$$\rho_m = \alpha_v \rho_v + (1 - \alpha_v)\rho_l, \tag{7}$$

$$\mu_m = \alpha_v \mu_v + (1 - \alpha_v)\mu_l, \tag{8}$$

where α_v is the vapor volume fraction; ρ_l and ρ_v represent the density of liquid and vapor, respectively; μ_l and μ_v are the liquid and vapor dynamic viscosities, respectively.

3.1.2. Cavitation model

With the development of CFD technology, the research on cavitation in fluids is progressing continuously. Scholars have proposed various cavitation models based on the R–P equation (Alehossein and Qin, 2007; Qin et al., 2007). Singhal model (Singhal et al., 2002), Schnerr and Sauer model (Schnerr and Sauer, 2001) and Zwart-Gerber-Belamri model (Zwart et al., 2004) are three typical cavitation models, which have been embedded in Fluent 19.0 software and have been widely used.

Among the three cavitation models, Schnerr and Sauer models are more suitable for simulating cavitation flow in holes because its advantages in the stability and convergence when calculating pressure coefficient (Lei et al., 2015). In addition, Chen et al. (2019) found that the cavitation jet simulation result error was the smallest in the Schnerr and Sauer model. Hence, the Schnerr and Sauer cavitation model is used to describe the self-resonant cavitation jet flow field according to the actual situation of the research process in this study.

$$\frac{\partial}{\partial t}(\alpha_v \rho_v) + \frac{\partial}{\partial x_j}(\alpha_v \rho_v u_j) = R_e - R_c \tag{9}$$

$$R_e = \frac{\rho_v \rho_l}{\rho_m}\alpha_v(1 - \alpha_v)\frac{3}{R}\sqrt{\frac{2(P_v - P_\infty)}{3\rho_l}}, \quad \text{when } P_v \geq P \tag{10}$$

$$R_c = \frac{\rho_v \rho_l}{\rho_m}\alpha_v(1 - \alpha_v)\frac{3}{R}\sqrt{\frac{2(P_\infty - P_v)}{3\rho_l}}, \quad \text{when } P_v \leq P \tag{11}$$

where R_e and R_c represent the evaporation and condensation of the vapor bubbles, respectively; P_v and P_∞ are respectively the saturation vapor pressure and local-far field pressure; and R represents the radius of bubble.

3.1.3. Turbulence model

Reynolds Average Navier-Stokes (RANS) is a widely used turbulence model in industrial flow calculation at present, with its advantages in wide application range, accuracy and computational efficiency. It mainly includes $k - \varepsilon$ and $k - \omega$ turbulence models, among which $k - \varepsilon$ includes three different forms: Standard $k-\varepsilon$ model, RNG $k - \varepsilon$ model and Realizable $k - \varepsilon$ model; while $k - \omega$ turbulence models include Standard $k - \omega$ model and SST $k - \omega$ model.

In the previous research literature (Celik et al., 2014; Yao et al., 2014), the RNG $k - \varepsilon$ model has been proved to be effective in CFD cavitation simulation. Moreover, a comparison has been made with the same Schnerr–Sauer cavitation model between different turbulence models, which are Standard $k - \varepsilon$, RNG $k - \varepsilon$, Realizable $k - \varepsilon$, Standard $k - \omega$ and SST $k - \omega$ (Chen et al., 2019). The results indicate that the result of the RNG $k - \varepsilon$ model has the smallest error with Yao et al. (2014) and is suitable for cavitation simulation. Therefore, the RNG $k - \varepsilon$ model is adopted to simulate the flow characteristic of cavitation.

$$\frac{\partial(\rho k)}{\partial t} + \frac{\partial(\rho k u_i)}{\partial x_i} = \frac{\partial}{\partial x_j}\left[\alpha_k \mu_{eff}\frac{\partial k}{\partial x_j}\right] + G_k + \rho\varepsilon \tag{12}$$

$$\frac{\partial(\rho\varepsilon)}{\partial t} + \frac{\partial(\rho\varepsilon u_i)}{\partial x_i} = \frac{\partial}{\partial x_j}\left[\alpha_\varepsilon \mu_{eff}\frac{\partial\varepsilon}{\partial x_j}\right] + \frac{C_{1\varepsilon}^*\varepsilon}{k}G_k - C_{2\varepsilon}\rho\frac{\varepsilon^2}{k} \tag{13}$$

with

$$\left.\begin{aligned}
&\mu_{eff} = \mu + \mu_t \\
&\mu_t = \rho C_\mu \frac{k^2}{\varepsilon} \\
&C_\mu = 0.0845, \quad \alpha_k = \alpha_\varepsilon = 1.39 \\
&C_{1\varepsilon}^* = C_{1\varepsilon} - \frac{\eta(1 - \eta/\eta_0)}{1 + \beta\eta^3} \\
&C_{1\varepsilon} = 1.42, \quad C_{2\varepsilon} = 1.68 \\
&\eta = (2E_{ij}\cdot E_{ij})^{1/2}\frac{k}{\varepsilon} \\
&E_{ij} = \frac{1}{2}\left(\frac{\partial u_i}{\partial x_j} + \frac{\partial u_j}{\partial x_i}\right) \\
&\eta_0 = 4.377, \quad \beta = 0.012
\end{aligned}\right\} \tag{14}$$

where G_k is the generation of turbulent kinetic energy by the mean velocity gradients; $C_{1\varepsilon}$ and $C_{2\varepsilon}$ are the empirical constants; α_k and α_ε are the reciprocal of the effective turbulent Prandtl number of the turbulent kinetic energy k and the dissipation rate ϵ, respectively.

3.2. Computational domain

In previous studies (Hutli et al., 2016; Lei et al., 2015), the two-dimensional model can describe the flow field characteristics of the actual model ignoring the Z-direction velocity, and the cylindrical symmetric nozzle can generate the average jet axisymmetric velocity profile in the two-dimensional plane, and the simulation results are in good agreement with the experimental results. For simplification and better computational efficiency, the two-dimensional rotating cross section of the actual model is used instead of the actual geometric model to simulate the cylindrical symmetrical nozzle. Since the cavitation nozzle is a cylindrical symmetrical structure, the two-dimensional axisymmetric model is chosen as the research target, while the fluid velocity in the Z direction is ignored. Fig. 5 shows the two-dimension model used in this study. The length and width of the outflow field are all set as 15d, which meet the flow field boundary of submerged free jet and eliminate the influence of flow field boundary on the simulation results.

3.3. Simulation setup

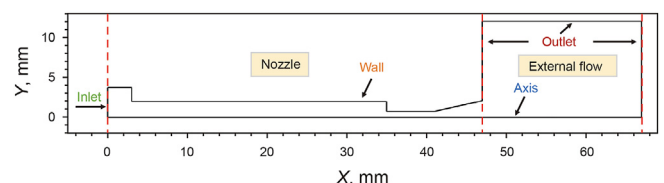SIMPLEC algorithm and finite volume method in Fluent 19.0

Fig. 5. The two-dimensional computational domain.

were used to discretize the equations. Based on the Reynolds time-mean N−S equation, the momentum equation and turbulent transport equation were discretized by the second-order upwind difference scheme, and the diffusion term was discretized by the central difference scheme. PRESTO! scheme is used for the pressure interpolation of continuity equation, and Quick scheme is used for the convection term of vapor volume fraction equation. The inlet boundary condition of the nozzle is Pressure-Inlet, and the pressure value is 4 MPa. The outlet boundary condition is fixed zero pressure at outlet. The nozzle boundary is set as wall boundary condition, and the axis of the geometric model is set as the axis boundary condition. The nozzle and wall are regarded as no-slip walls. The jet turbulence intensity at the inlet and outlet is set at 5%, and the reference pressure is 101325 Pa. The saturated vapor pressure of water is set as 3540 Pa at 300 K. Additionally, it is worth mentioning that in the unsteady calculation, the time step $\Delta T = 0.000001$ s is selected to meet the requirements of the Courant number in the calculation process, and the slip velocity is ignored in the calculation models.
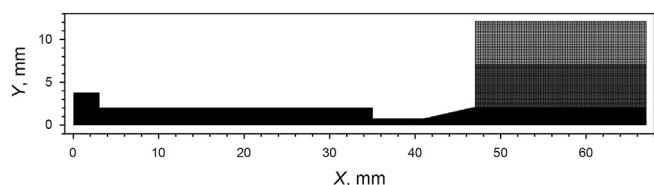
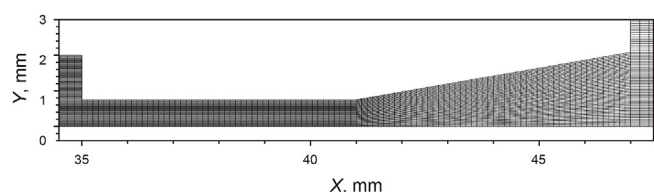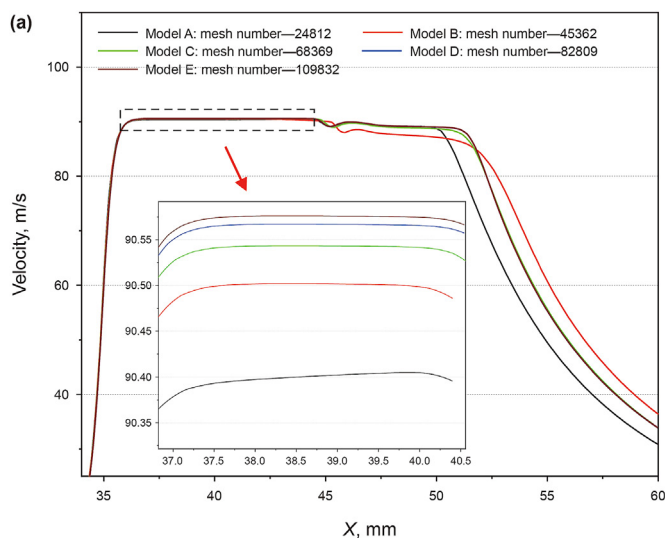**Fig. 6.** Mesh strategy of computational domain.

Fig. 7. Detail mesh near the nozzle throat.

3.4. Mesh selection

In this study, the computational domain was partitioned into blocks to generate quadrilateral structured grids with good orthogonality, as shown in Fig. 6. Due to the small size and high jet velocity in the nozzle, a high quality and high-density mesh structure is needed. Therefore, the mesh in the nozzle is refined to improve the calculation accuracy, as shown in Fig. 7. The quadrilateral grid is adopted mainly because the model to be calculated has an obvious main flow direction, that is, along the direction of the nozzle axis, the quadrilateral grid with an edge perpendicular to the direction of the inflow is conducive to ensuring that the conservation of the equation is satisfied.

Sensitivity analyses with 5 different mesh models (A-E) are conducted to test the mesh effect on the simulation results. From mesh model A to mesh model E, the number of grids is 24812, 45362, 68369, 82809, and 109832, respectively. Numerical simulation of cavitation jet was carried out for the nozzle geometric model with different mesh numbers. The velocity and pressure distribution on the axis line and the vapor volume distribution on the line $Y = 0.749$ mm (nozzle throat wall) are extracted from each calculation example. The mesh effects on simulated velocity, pressure and volume fraction of vapor are shown in Figs. 8−10. The distribution curves of velocity, pressure, and vapor volume gradually reach the asymptotic value with the increase in mesh number. When the number of grids increased from 82809 to 109832, the velocity, pressure, and vapor volume fraction only increased by 0.9%, 0.007% and 0.04%, respectively. Therefore, 82,809 grid cells are selected to meet the computational accuracy requirements in this study. Herein, the mesh model D with mesh number 82809 is selected for a balance of computational efforts and accuracy. Moreover, the average orthogonal quality is 0.966, which indicates that the grid used is of good quality for the application of CFD numerical simulation.

3.5. Model validation

Since cavitation initiation is difficult to distinguish from cavitation development, the cavitation cloud period can be considered
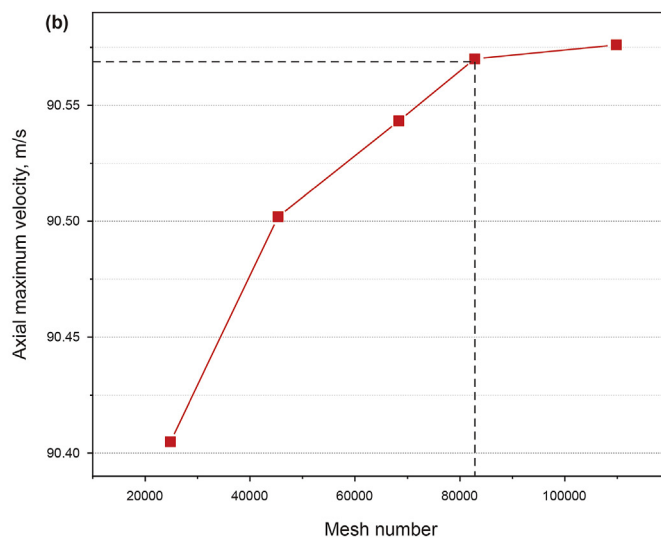

Fig. 8. Grid-independence analysis: (**a**) distribution curves of velocity and (**b**) grid sensitivity of axial maximum velocity.
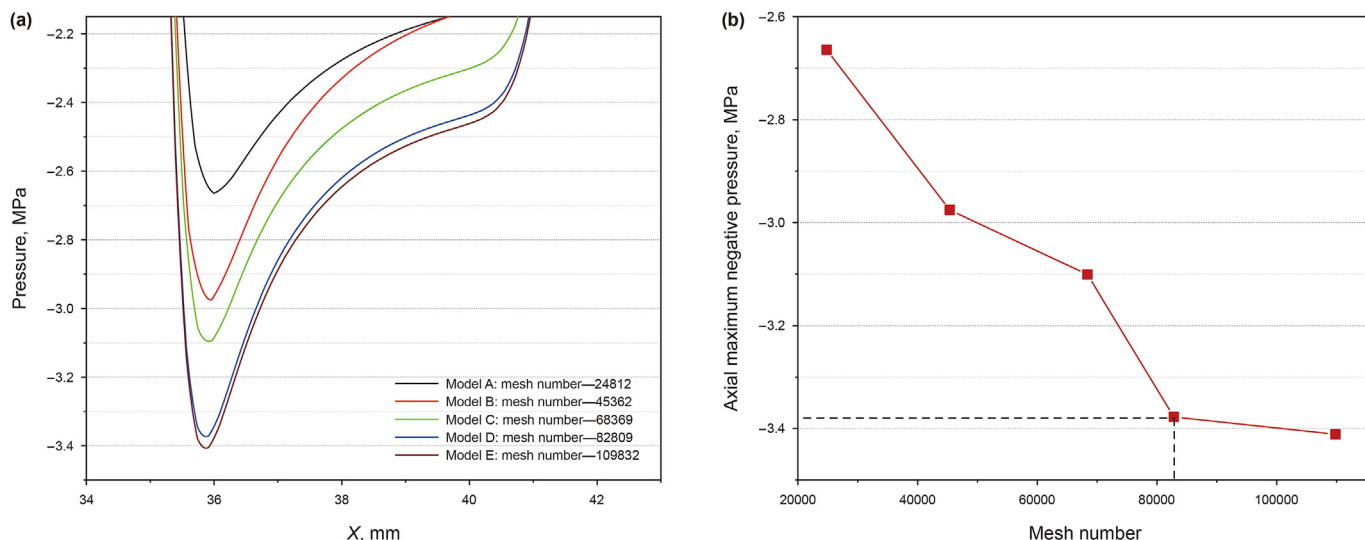
Fig. 9. Grid-independence analysis: (**a**) distribution curves of pressure and (**b**) grid sensitivity of axial maximum negative pressure.
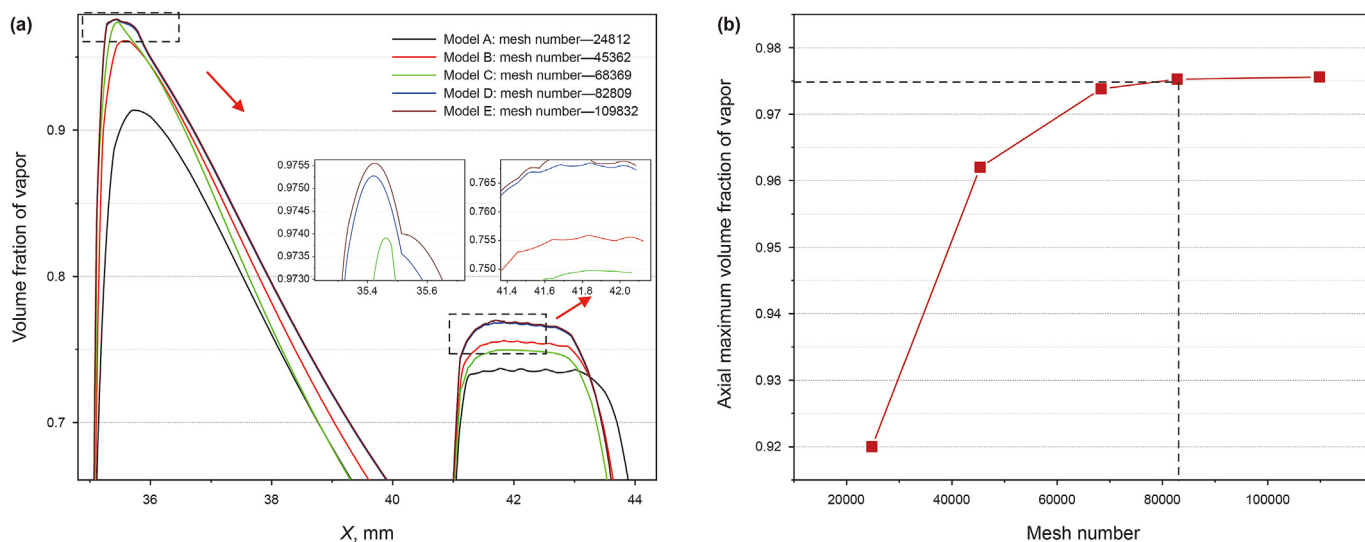

Fig. 10. Grid-independence analysis: (**a**) distribution curves of volume fraction of vapor and (**b**) grid sensitivity of axial maximum vapor volume fraction.

to include three predominant processes: development, shedding and collapse of cavitation. In order to observe the initial position of cavitation cloud in the visualization experiment, the jet displacement is gradually increased to the initial position of cavitation. To compare with the experimental results, the transient solution is employed to obtain the variation of cavitation clouds with time.

Fig. 11 and Fig. 12 shows the experimental and simulated results of cavitation clouds over time, respectively. It can be observed from Fig. 11 that cavitation initiation occurs at $t = 0$, while in Fig. 12 the cavitation initiation is delayed to $t = 20$ μs, it may be attributed to the deviation between the initial calculation conditions of the numerical model and the experimental conditions. In Fig. 11, the initial position A is located at the beginning of the nozzle throat and divergent section, that is, the boundary layer separation leading

edge, which is consistent with the simulated results in Fig. 12. Then the cavitation bubbles continue to expand and interact with each other until $t = 350$ μs, forming bubbly bulges similar to the hydrofoil cavitation. The bulges migrate rapidly downward and cluster together into clouds. A similar phenomenon can be seen from the cavitation clouds at $t = 380$ μs in Fig. 12. Additionally, the migration velocity of the cavitation clouds is calculated. From $t = 50$ μs to $t = 150$ μs, the migration distance is 5 mm and the velocity is calculated to be 50 m/s when $t = 150$ μs. Similarly, the velocity is calculated to be 30 m/s at $t = 350$ μs. Compared with the simulated results in Fig. 13(a), the migration velocity of cavitation clouds is consistent with the cavitating jet velocity, which illustrates the accuracy of the simulated results. The cavitation clouds continue to migrate downwards and it is found that B ($t = 500$ μs)
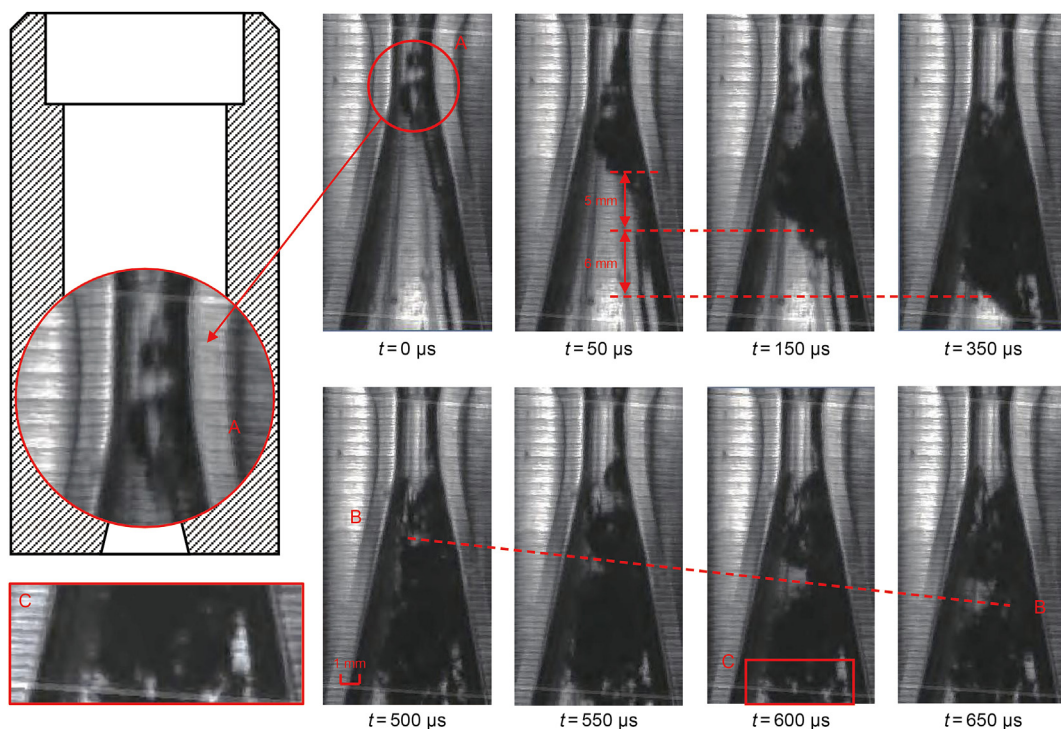
Fig. 11. Morphological changes of cavitation clouds in a single cycle. Region A shows the cavitation initiation. Line B indicates the location of the separation of the cavitation cloud. In Region C, all the bubbles collapse. The red dot at A is the bubble core (Tan et al., 2022).

begins to fall off and the shedding position gradually dilates as it moves downwards. This phenomenon is considered as an upward reverse jet generated at the shedding position B, which collides with the mainstream, leading to the gradual separation of the cavitation cloud and the nozzle. The large-scale shedding of the cavitation cloud will occur as the fluid flows in the direction of the liquid flowing out of the cavity (Kawanami et al., 1997; Callenaere et al., 2001; Wang et al., 2012). Shock wave theory is another explanation of the phenomenon of cavitation cloud shedding. It is believed that a large number of cavitation clouds at the nozzle outlet collapse rapidly, resulting in water vapor shock wave, and when the pressure wave is transmitted upward to the front edge of cavitation cloud in the next period, cavitation cloud shedding in two cycles will be formed (Ganesh et al., 2016; Roger et al., 2006). The shock wave effect cannot be ignored when the flow rate is fast and the cavitation number is small. The detached cavitation clouds continue to migrate downwards to C, and a large number of cavitation clouds collapse, accompanied by a rapid decrease in volume until completely disappeared. In the self-resonant cavitation device, the reverse jet is generated because the higher flow velocity leads to the larger negative pressure in the nozzle throat and the entrapment of the fluid near the wall in the expansion section. It can be seen from the velocity flow diagram in Fig. 13(b) that the arrows inconsistent with the direction of the mainstream arrows on the wall surface represent the reverse jet flow. This result confirms the phenomenon of cavitation cloud shedding observed in the experiment from the perspective of numerical simulation.

4. Results and discussion

4.1. Influence of throat length on cavitation cloud

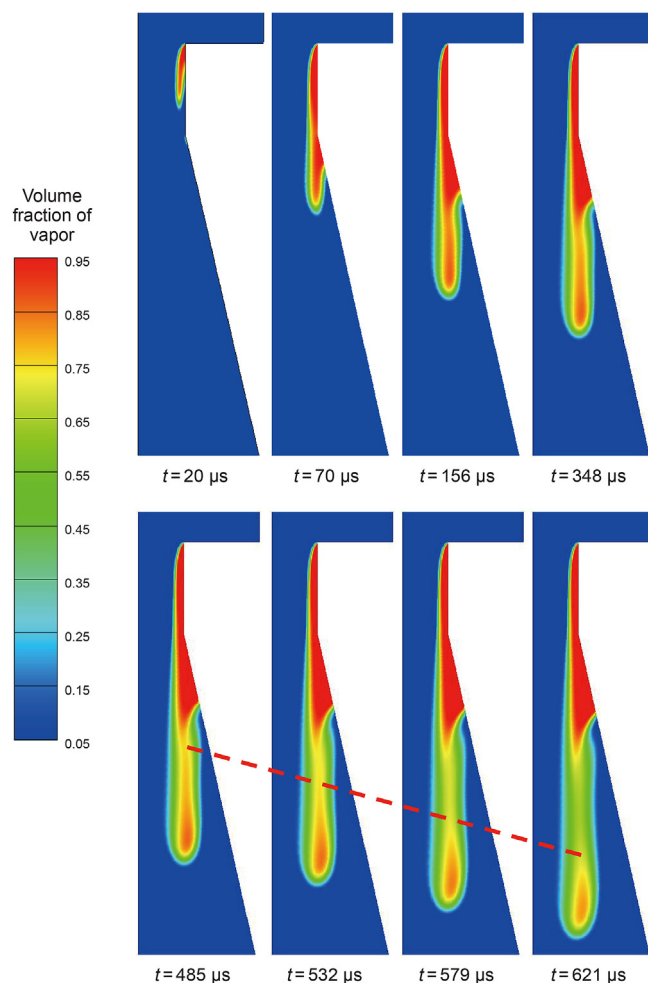In this section, the influence of throat length on cavitation effect
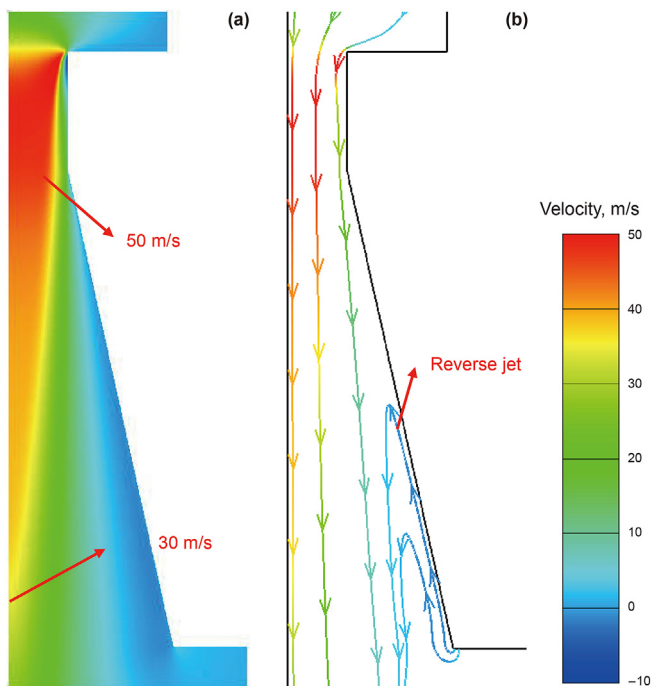

Fig. 12. The variation of cavitation clouds with time.

Fig. 13. Velocity characteristic: (**a**) velocity contour and (**b**) path line.
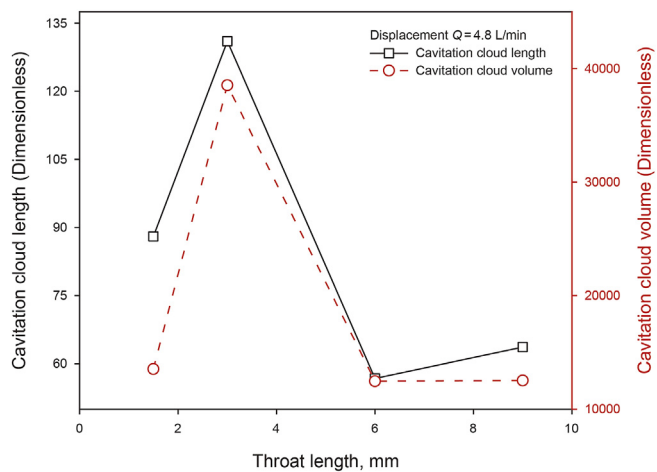

Fig. 14. The length and volume of cavitation cloud varies with throat length *l*.

is discussed. The experiment and simulation in this group involve nozzles with throat length of 1.5, 3.0, 6.0, and 9 mm, and other parameters are shown in Table 1.

As illustrated in Fig. 14, by comparing the average length and volume of the cavitation cloud of each nozzle, when the throat length is 3.0 mm (twice of the throat diameter), the maximum average length and volume of the jet cavitation cloud can be obtained.

Combined with the periodic variation of cavitation jet in Fig. 11, it can be seen that the initial position of cavitation is the leading edge of the extension section. If the throat section is too short, the
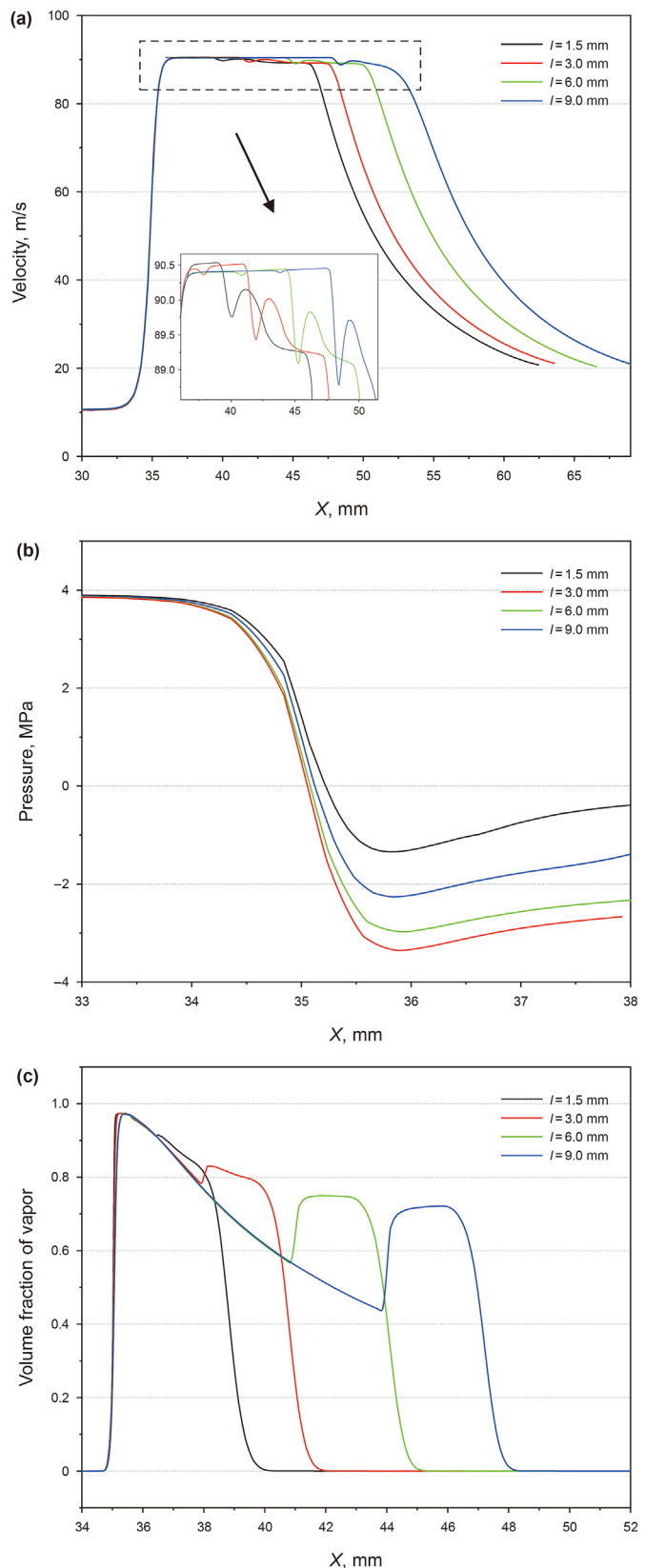

Fig. 15. The flow field characteristics varies with throat length *l*: (**a**) velocity distribution, (**b**) pressure distribution, and (**c**) vapor distribution.
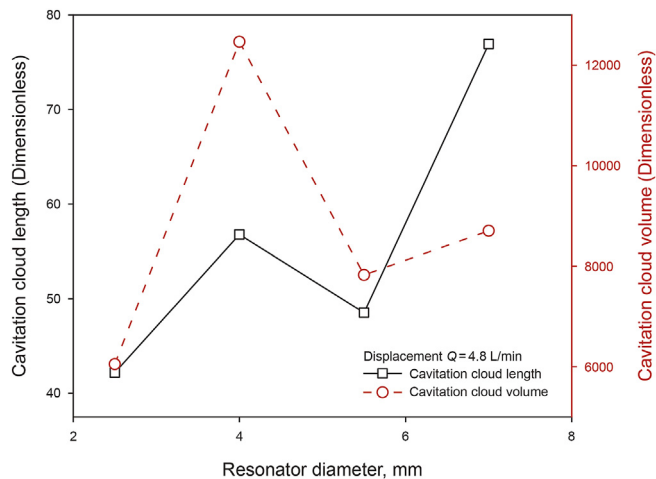
Fig. 16. The length and volume of cavitation cloud varies with resonator diameter *D*.

jet cannot fully realize boundary layer separation and form cavitation clouds at this position due to inertia. However, if the throat section is too long, the jet energy in the throat section decreases rapidly due to the small throat diameter and low pump pressure, which weakens the cavitation effect. As can be seen from Fig. 15(a), when the throat length is 3 mm, a larger velocity value and distribution range can be maintained at the throat, which is most conducive to the migration of cavitation clouds, thus generating a larger length of cavitation clouds. Meanwhile, the negative pressure generated at the throat is the largest (Fig. 15(b)), and the volume fraction and distribution range of cavitation cloud are the largest (Fig. 15(c)), thus forming a larger volume of cavitation cloud.

4.2. Influence of resonator diameter on cavitation cloud

In this section, the influence of resonator diameter on cavitation effect is discussed. This group of experiments and mathematical models involve nozzles with resonator diameters of 2.5, 4.0, 5.5, and 7.0 mm, respectively, and other parameters are shown in Table 1.

It can be seen from Fig. 16 that the increase in resonator diameter is beneficial to migration of cavitation clouds, and the length of cavitation cloud has maximum value at $D = 7.0$ mm. The volume of cavitation cloud increases first and then decreases as the resonator diameter increases, and reaches its maximum when $D = 4.0$ mm.

The change of the average volume of cavitation cloud with a single nozzle has the trend as the average length, that is, it increases with the increase in displacement. Among the four nozzles tested (2.5, 4.0, 5.5, and 7.0 mm), $D = 4.0$ mm leads to the largest cavitation volume. This is consistent with the simulation results in Fig. 17(b) and (c). When $D = 4.0$ mm, the negative pressure and vapor volume fraction generated inside the nozzle are both the maximum, which makes it easy to form a larger volume of cavitation cloud. The average length of cavitation cloud in $D = 5.5$ mm group and $D = 4.0$ mm group is similar, but the volume of cavitation cloud of $D = 5.5$ mm group is small, indicating that the cavitation cloud is not fully developed in the process of jet flow. Compared with $D = 7.0$ mm and $D = 4.0$ mm, the cavitation cloud migration length of $D = 7.0$ mm nozzle is longer, but the volume of cavitation cloud generated is smaller, indicating that the cavitation
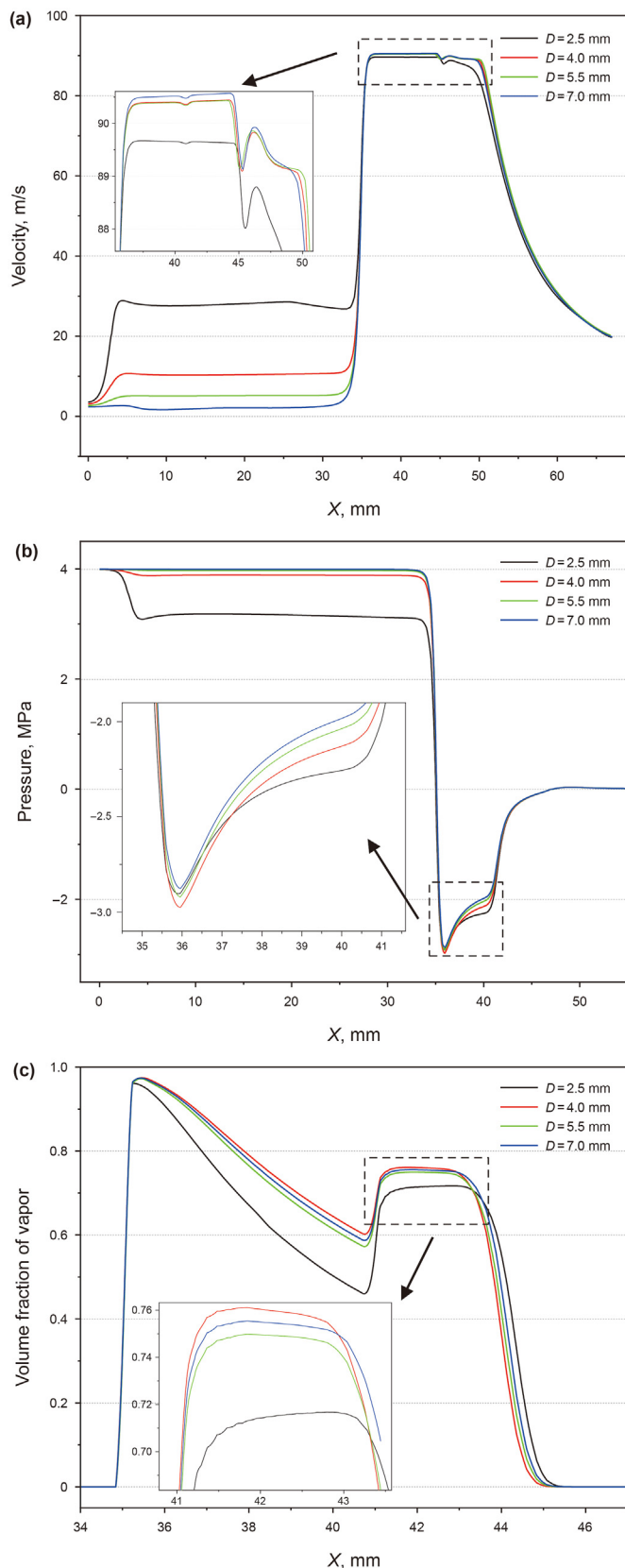

Fig. 17. The flow field characteristics varies with resonator diameter *D*: (**a**) velocity distribution, (**b**) pressure distribution, and (**c**) vapor distribution.
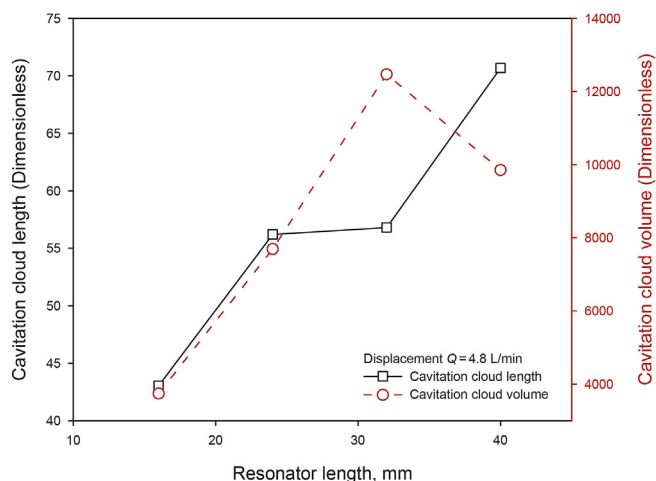
Fig. 18. The length and volume of cavitation cloud varies with resonator length *L*.

cloud has partially collapsed before migration to the maximum distance in this process.

4.3. Influence of resonator length on cavitation cloud

In this section, the influence of resonator length on cavitation effect is discussed. The length of the nozzle resonator is 16 mm, 24 mm, 32 mm and 40 mm respectively, and other parameters are shown in Table 1.

As shown in Fig. 18, prolonging the length of the resonator leads to a larger cavitation cloud length, indicating that prolonging the length of the resonator is conducive to cavitation bubble migration. Additionally, it can be found that the volume of cavitation cloud of the nozzle *L* = 32 mm is the largest, indicating that serious collapse phenomenon occurs when the resonator length exceeds 32 mm.

As illustrated by Fig. 19 (b) and (c), when *L* = 32 mm, the nozzle throat produces the largest negative pressure and the strongest resonance effect, which is easier to stimulate fluid cavitation and produces the largest volume of cavitation cloud. Fig. 19 (a) shows that the nozzle *L* = 40 mm possesses the maximum axial velocity and is conducive to cavitation cloud migration, which is also consistent with the experimental results shown in Fig. 18.

4.4. Influence of divergent angle on cavitation cloud

In this section, the influence of exit divergent angle on cavitation effect is discussed. The experiment and simulation involve nozzles with divergent angle of 10°, 25°, 40°, and 55°, and other parameters are shown in Table 1.

As can be seen from Fig. 20, the nozzle of α = 10° has the maximum cavitation cloud length. From Fig. 21(a), it can be seen that the nozzle of α = 10° forms the longest potential core, and increases the migration distance of cavitation clouds. By comparing the average volume of cavitation clouds at each nozzle, when the divergent angle is 40°, the volume of cavitation cloud increases more significantly compared with other nozzles, as shown in Fig. 20. In Fig. 21, the divergent angle affects the pressure distribution of the jet field more. The negative pressure value and vapor volume fraction at the throat both reach the maximum when α =
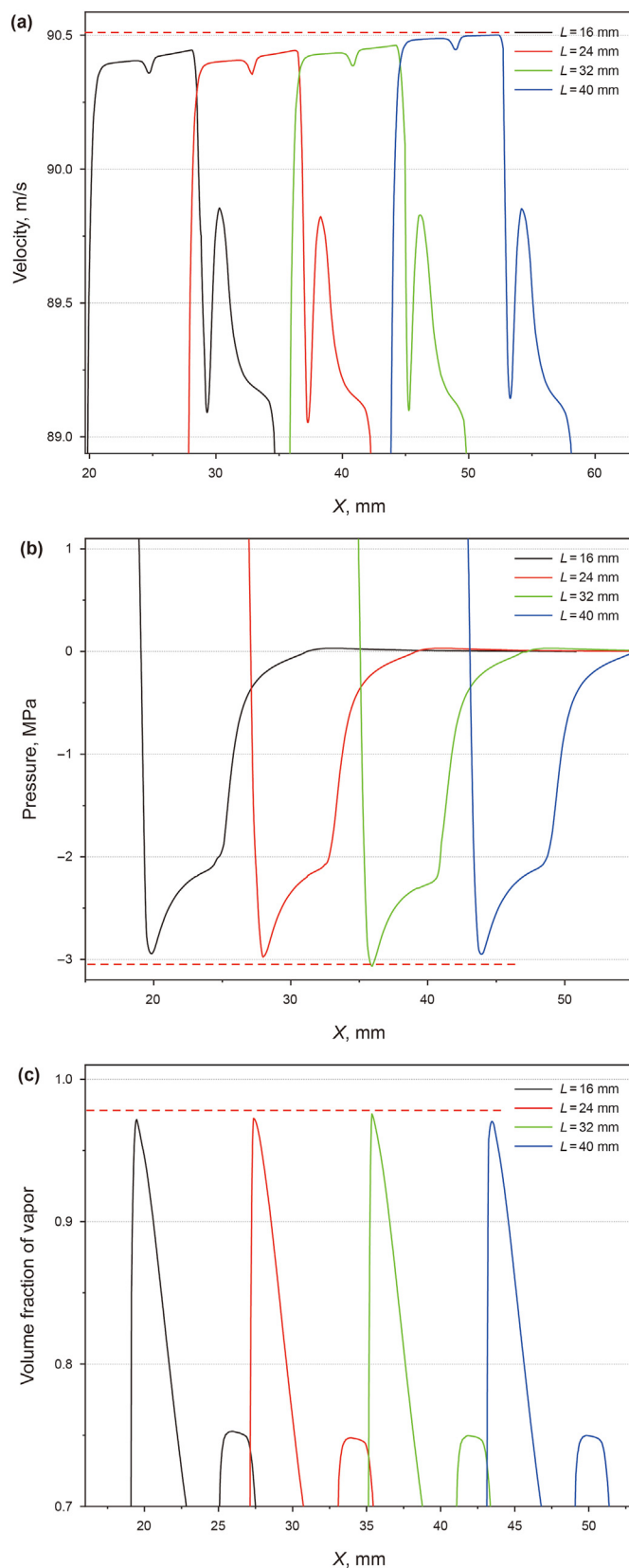

Fig. 19. The flow field varies with resonator length *L*: (**a**) velocity distribution, (**b**) pressure distribution and (**c**) vapor distribution.
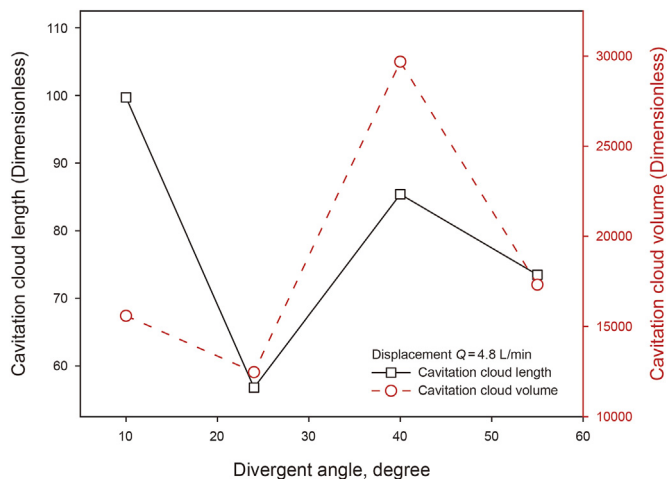
Fig. 20. The length and volume of cavitation cloud varies with divergent angle α.

$40°$, which is most conducive to the generation and development of cavitation clouds.

5. Conclusions

Visualization experiments and numerical simulation methods are used to investigate the effects of sizes of self-resonant cavitation nozzles on cavitation jet capacity and cavitation jet flow field. The influences of the four key parameters, including resonator diameter, resonator length, throat length and divergent angle, on the length and volume of cavitation cloud and velocity, pressure and vapor distribution characteristic are studied, and the conclusions are:

(1) The length of resonator should be designed according to the hydraulic parameters of specific working conditions so that the nozzle natural frequency is close to the jet excitation frequency. Proper extension of resonator length is beneficial to cavitation migration, and the specific extension distance should consider whether the application environment needs a larger erosion range or a stronger erosion effect.

(2) The increase in resonator diameter is beneficial to migration of cavitation clouds. Different from that, the volume of cavitation clouds has maximum value at $D = 4.0$ mm, and the maximum negative pressure value and vapor volume fraction are gained.

(3) In present study, the experimental and simulation results show that the optimal throat length is twice of the throat diameter. Under this condition, the maximum average length and volume of the jet cavitation cloud can be obtained.

(4) The divergent angle of the nozzle mainly affects the pressure distribution of the jet flow field. The optimal value of divergent angle is $40°$ in present experimental and simulation results.

Declaration of competing interest

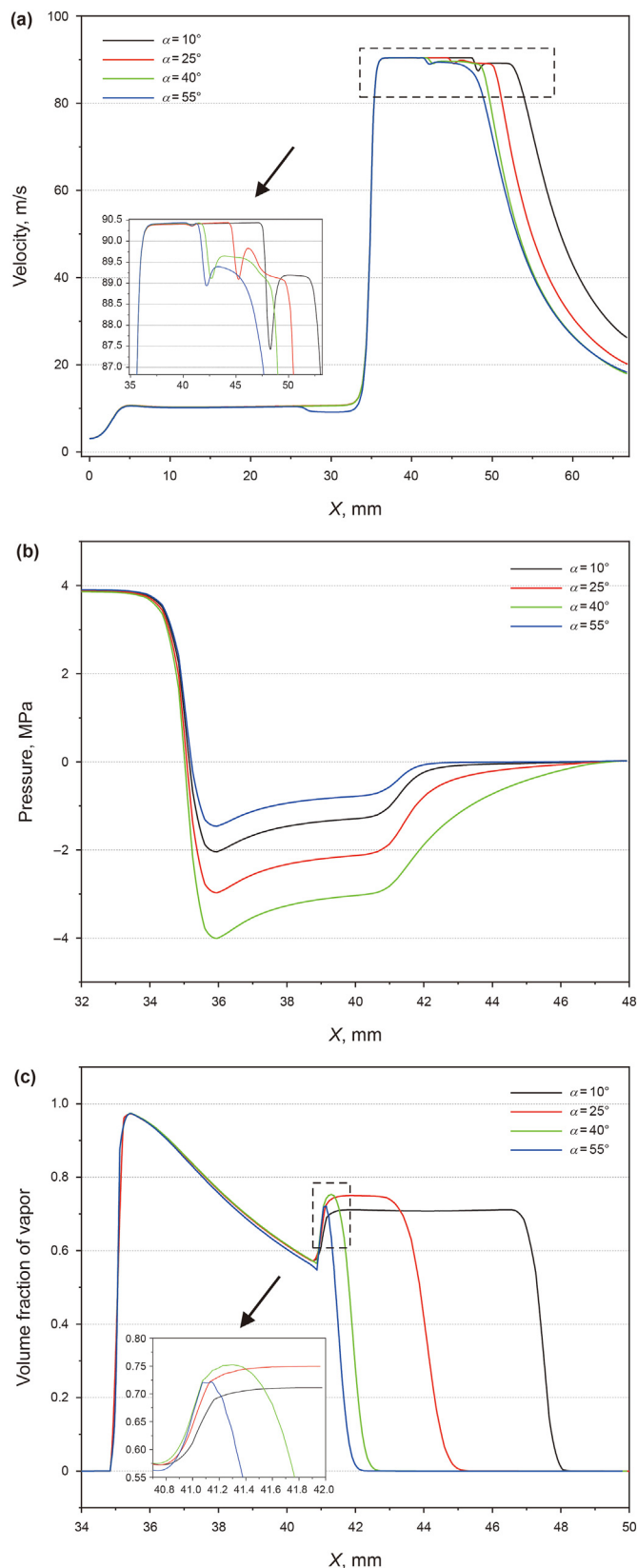No potential conflict of interest was reported by the authors.

Fig. 21. The flow field characteristics varies with divergent angle α: (**a**) velocity distribution, (**b**) pressure distribution and (**c**) vapor distribution.

Acknowledgements

References

Alehossein, H., Qin, Z., 2007. Numerical analysis of Rayleigh-Plesset equation for cavitating water jets. Int. J. Numer. Methods Eng. 72 (7), 780—807. https://doi.org/10.1002/nme.2032.

Callenaere, M., Franc, J.P., Michel, J.M., et al., 2001. The cavitation instability induced by the development of a re-entrant jet. J. Fluid Mech. 444, 223—256. https://doi.org/10.1017/S0022112001005420.

Celik, F., Ozden, Y.A., Bal, S., 2014. Numerical simulation of the flow around two-dimensional partially cavitating hydrofoils. J. Mar. Sci. Appl. 13 (3), 245—254. https://doi.org/10.1007/s11804-014-1254-x.

Cen, L., Wang, J.Q., Zhu, X.J., 2018. The acoustic cavitation field distribution in power ultrasonic honing by hydrophone method. Sci. Technol. Eng. 18 (4), 23—28 (in Chinese).

Chahine, G.L., Hsiao, C.T., Raju, R., 2014. Scaling of cavitation bubble cloud dynamics on propellers. Fluid Mech. Appl. 106, 345—373. https://doi.org/10.1007/978-94-017-8539-6_15.

Chen, Y., Li, J., Gong, Z.X., et al., 2018. Large eddy simulation and investigation on the laminar-turbulent transition and turbulence-cavitation interaction in the cavitating flow around hydrofoil. Int. J. Multiphas. Flow 112, 300—322. https://doi.org/10.1016/j.ijmultiphaseflow.2018.10.012.

Chen, Y.Z., Hu, Y.H., Zhang, S.L., 2019. Structure optimization of submerged water jet cavitating nozzle with a hybrid algorithm. Eng. Appl. Comput. Fluid. Mech. 13 (1), 591—608. https://doi.org/10.1080/19942060.2019.1628106.

Gaitan, Felipe, D., 1992. Sonoluminescence and bubble dynamics for a single, stable, cavitation bubble. J. Acoust. Soc. Am. 91 (6), 3166—3183. https://doi.org/10.1121/1.402855, 1992.

Ganesh, H., Mǎkiharju, S.A., Ceccio, S.L., 2016. Bubbly shock propagation as a mechanism for sheet-to-cloud transition of partial cavities. J. Fluid Mech. 802, 37—78. https://doi.org/10.1017/jfm.2016.425.

Hutli, E., Nedeljkovic, M.S., Radovic, N.A., et al., 2016. The relation between the high speed submerged cavitating jet behaviour and the cavitation erosion process. Int. J. Multiphas. Flow 83, 27—38. https://doi.org/10.1016/j.ijmultiphaseflow.2016.03.005.

Kawanami, Y., Kato, H., Yamaguchi, H., et al., 1997. Mechanism and control of cloud cavitation. J. Fluid Eng. 119 (4), 788—794. https://doi.org/10.1115/1.2819499.

Lei, C.C., Deng, S.S., Guan, J.F., et al., 2015. Flow field numerical simulation and erosion experiment research of submerged cavitating water jets. J. Chongqing. Univ. Technol. (Nat. Sci.) 29 (12), 71—76 (in Chinese).

Li, D., Kang, Y., Ding, X.L., et al., 2016. Experimental study on the effects of feeding pipe diameter on the cavitation erosion performance of self-resonating cavitating waterjet. Exp. Therm. Fluid Sci. 87, 314—325. https://doi.org/10.1016/j.expthermflusci.2016.11.029, 2016.

Li, G.S., Shen, Z.H., Zhang, Z.P., et al., 2003. Development and field tests of self-resonating cavitating water jet nozzle for oilwell drilling. Petrol. Drill. Tech. 31 (5), 11—13, 2003, (in Chinese).

Li, G.S., Shen, Z.H., 1992. Design principle of organ-pipe cavitating jet nozzles. J. China Univ. Petrol. 16 (5), 35—39 (in Chinese).

Li, G.S., Shen, Z.H., 1996. Investigation and application of cavitating water jet in drilling. Petrol. Drill. Tech. 24 (4), 54—57+65 (in Chinese).

Liao, H.L., Zhao, S.L., Cao, Y.F., et al., 2020. Erosion characteristics and mechanism of the self-resonating cavitating jet impacting aluminum specimens under the confining pressure conditions. J. Hydrodyn. 32, 375—384. https://doi.org/10.1007/s42241-020-0024-2.

Lindau, J.W., Boger, D.A., Medvitz, R.B., et al., 2005. Propeller cavitation breakdown analysis. J. Fluid Eng. 127 (5), 995—1002. https://doi.org/10.1115/1.1988343.

Liu, B., Cai, J., Li, F.C., et al., 2013. Simulation of heat transfer with the growth and collapse of a cavitation bubble near the heated wall. J. Therm. Sci. 22 (4), 352—358. https://doi.org/10.1007/s11630-013-0635-9.

Liu, B., Ma, F., 2021. Erosion behavior of aluminum by an inclined cavitating jet. Wear 474—475, 203751. https://doi.org/10.1016/j.wear.2021.203751.

Liu, B., Pan, Y., Ma, F., 2020. Pulse pressure loading and erosion pattern of cavitating jet. Eng. Appl. Comput. Fluid. Mech. 14 (1), 136—150. https://doi.org/10.1080/19942060.2019.1695675.

Liu, X.H., Fang, K.L., 2004. A difference image algorithm for target positioning based on profile projection. Comput. Appl. Softw. 7, 87—88 (in Chinese).

Peng, C., Tian, S.C., Li, G.S., 2018. Joint experiments of cavitation jet: high-speed visualization and erosion test. Ocean Eng. 149, 1—13. https://doi.org/10.1016/j.oceaneng.2017.11.009.

Peng, G.Y., Shimizu, S., 2013. Progress in numerical simulation of cavitating water jets. J. Hydrodyn. 25 (4), 502—509. https://doi.org/10.1016/S1001-6058(11)60389-3.

Peng, G.Y., Yang, C.X., Oguma, Y., 2016. Numerical analysis of cavitation cloud shedding in a submerged water jet. J. Hydrodyn. 28 (6), 986—993. https://doi.org/10.1016/S1001-6058(16)60700-X.

Peng, K.W., Li, G.S., Tian, S.C., et al., 2017. Triggering cavitation in multilateral coiled tubing drilling by high pressure water jet. SPE/IATMI Asia Pac. Oil Gas Conf. Exhibit. https://doi.org/10.2118/186380-MS.

Peng, K.W., Tian, S.C., Li, G.S., et al., 2018. Mapping cavitation impact field in a submerged cavitating jet. Wear 396, 22—33. https://doi.org/10.1016/j.wear.2017.11.006.

Qin, Z., Bremhorst, K., Alehossein, H., et al., 2007. Simulation of cavitation bubbles in a convergent—divergent nozzle water jet. J. Fluid Mech. 573, 1—25. https://doi.org/10.1017/S002211200600351X, 2007.

Roger, A., Martin, W., Qiao, Q., 2006. Experimental and numerical investigation of large scale structures in cavitating wakes. In: 36th AIAA Fluid Dynamics Conference.

Schnerr, G.H., Sauer, J., 2001. Physical and numerical odelling of unsteady cavitation dynamics. In: 4th International Conference on Multiphase Flow.

Shen, X.M., Li, G.S., Ma, J.J., et al., 1996. Study on scaling mechanism and hydraulic cleaning technology of tubing. Petrol. Drill. Tech. 3, 44—46 (in Chinese).

Shi, H.B., Li, M.D., Nikrityuk, P., et al., 2019. Experimental and numerical study of cavitation flows in venturi tubes: from CFD to an empirical model. Chem. Eng. Sci. 207, 672—687. https://doi.org/10.1016/j.ces.2019.07.004.

Singhal, A.K., Athavale, M.M., Li, H.Y., et al., 2002. Mathematical basis and validation of the full cavitation model. J. Fluid Eng. 124 (3), 617—624. https://doi.org/10.1115/1.1486223.

Tan, Y.W., Zhang, Y.Q., Yu, C., et al., 2022. Evolution of the cavitation cloud and stability of flow fields in a cavitating jet. Petrol. Sci. Bull. 7 (1), 71—80 (in Chinese).

Wang, X.J., Li, G.S., Kang, Y.J., et al., 2009. Improvement of penetration rate with hydraulic pulsating-cavitation jet compound drilling technology. Acta Pet. Sin. 30 (1), 117—120 (in Chinese).

Wang, Y.W., Huang, C.G., Du, T.Z., et al., 2012. Shedding phenomenon of ventilated partial cavitation around an underwater projectile. Chin. Phys. Lett. 29 (1). https://doi.org/10.1088/0256-307X/29/1/014601.

Wu, J., Zhang, X.D., Liu, X.W., et al., 2003. Hydrodynamic cavitation and its applications. Chem. Ind. Eng. 6, 387—391 (in Chinese).

Xiang, L.H., Wei, X.S., Chen, S.Y., 2020. Experimental study on the frequency characteristics of self-excited pulsed cavitation jet. Eur. J. Mech. B Fluid 83, 66—72. https://doi.org/10.1016/j.euromechflu.2020.04.006, 2020.

Yao, L.M., Zhao, Y., Li, D.W., et al., 2014. Numerical research of the environmental influence of different depth on the shape of cavitation jet. Chin. J. Hydrodynam. 29 (6), 675—682 (in Chinese).

Yi, C., Li, G.S., Zhang, D.G., 2005. Experimental study on cavitation inception of nozzles with different geometries. J. Exp. Fluid Mech. 19 (1), 52—55+60 (in Chinese).

Zwart, P.J., Gerber, A.G., Belamri, T., 2004. A two-phase flow model for predicting cavitation dynamics. In: International Conference on Multiphase Flow.